Journal of Materials Research and Technology 27 (2023) 4738–4749

Contents lists available at ScienceDirect

Journal of Materials Research and Technology

journal homepage: www.elsevier.com/locate/jmrt

Effect of non-isothermal creep aging on the microstructure, mechanical properties and stress corrosion cracking resistance of 7075 alloy

Bo Jiang [a,b], Aoyun Fan [a,b], Fuhua Cao [c], Xiaoou Yi [d,*], Junhao Zhu [e], Shichen Li [e,**], Rui Liu [f]

[a] School of Materials Science and Engineering, Changzhou University, Changzhou, Jiangsu, 213164, China
[b] Jiangsu Key Laboratory of Materials Surface Science and Technology, Changzhou University, Changzhou, Jiangsu, 213164, China
[c] State Key Laboratory of Nonlinear Mechanics, Institute of Mechanics, Chinese Academy of Sciences, Beijing, 100190, China
[d] School of Materials Science and Engineering, University of Science and Technology Beijing, Beijing, 100083, China
[e] School of Materials Science and Engineering, Central South University, Changsha, 410083, China
[f] Anhui Xinhuai Electronic Co. Ltd, HuaiBei, 23500, China

ARTICLE INFO

Keywords:
Non-isothermal creep aging
SCC
Microchemical analysis
Precipitate

ABSTRACT

The effect of non-isothermal creep aging (NICA) on the microstructure, mechanical properties, and stress corrosion cracking (SCC) resistance of 7075 alloy was investigated. The results showed that the tensile strength of the alloy increased to 565 MPa when the alloy was heated to 210 °C (CH210) and reached 580 MPa when it was subsequently cooled to 120 °C (CC120). Simultaneously, the SCC susceptibility of r_{tf} increased from 50.8 % to 98.4 %. As compared with traditional creep aging process [1], a large strength increment with excellent stress corrosion resistance have been obtained by NICA. The microstructure revealed that a lot of dislocations have been introduced by creep during the heating stage which could improve the precipitates volume fraction and accelerate the diffusion of solutes; while during the cooling stage, η′ was greatly refined, and GPI and GPII were re-precipitated from the matrix due to the decreased solid solubility and increased critical radius R*; both of them are responsible for the continuous strength increase during NICA. Moreover, the width of the precipitate free zone (PFZ) was narrowed from 46.1 nm (CH210) to 28.6 nm (CC120). The microchemical analysis reveals that solutes were more homogenously distributed in grain boundary precipitates (GB-ppts), matrix precipitates, the PFZ, and the matrix with the help of creep. The narrower PFZ and homogeneous solute distribution are responsible for improving the SCC susceptibility in the CC120 alloy.

1. Introduction

Al–Zn–Mg–Cu alloys are widely used in the automotive and aircraft industries, for their low density, high strength and excellent fatigue resistance [1,2]. Creep age forming is a new aging process that aging and forming carried out simultaneously, it always used to produce parts with curved feature. It costs 18~48 h at 150 °C aging to achieve desirable mechanical properties and corrosion resistance [3,4]. The development of new creep aging processes is still of great value to improve mechanical properties and corrosion resistance with production time and cost reduction, production efficiency increase.

It is well known that mechanical properties and corrosion resistance of the material are tailored by alloy composition and aging technique by varying the microstructure in the grain interior and grainboundary. Tunable factors of microstructure include precipitate size, spatial distribution and chemical composition, solute atom segregation in precipitate free zones (PFZ), and the width of PFZ [5–7]. In Al–Zn–Mg–Cu alloys, GPI, GPII, η and η′ phases are the major precipitates formed during aging [8,9]. GPI is an ordered solute cluster formed along the $\{100\}_{Al}$ planes, featuring a size of 1–3 nm. GPII is a platelet of a few atomic layers along the $\{111\}_{Al}$ planes. GPI and GPII can provide nucleation sites for the η′ phase, which is important for strengthening. With increasing Zn concentration, the nucleation probability of GPI and GPII increases, along with an increase in the volume fraction of η′, thus giving rise to improved alloy strength [10]. However, the SCC resistance of these alloys decreased remarkably with increasing Zn concentration, due to the widened regimes of PFZ. Some works have demonstrated that the addition of Cu is beneficial for improving SCC resistance, and they

* Corresponding author.
** Corresponding author.
E-mail addresses: xiaoouyi@ustb.edu.cn (X. Yi), 740920844@qq.com (S. Li).

https://doi.org/10.1016/j.jmrt.2023.10.258
Received 12 July 2023; Received in revised form 3 October 2023; Accepted 25 October 2023
Available online 7 November 2023

found that the crack growth rate of the stress-independent region (stage II) decreased by two orders of magnitude, with increasing Cu content from 0.01 (wt.%) to 2.1 (wt.%) [11–13]. Noble Cu atoms can be incorporated into the grain boundary precipitates, reducing the potential difference between the grain boundary and its adjacent area, as well as the H content produced during cathodic reactions at the SCC crack tips [5]. However, high Cu content could also increase the alloy density and its susceptibility to hot-cracking.

In addition to chemical composition, age tempering has also been confirmed effective in altering precipitate chemistry and spatial distribution in Al–Zn–Mg–Cu alloys, providing an alternative route to material properties modification. For example, peak-aged alloys have shown combination of maximum tensile strength, but the worst corrosion resistance after T6 temper. T7 temper was developed to improve the corrosion resistance of alloys, however at a cost of strength reduction by 10–30 %. In recent years, a number of complex tempering methods have also been developed for Al–Zn–Mg–Cu alloys. A regression re-aging (RRA) temper developed by Cina et al. [14] demonstrated simultaneous improvement in the mechanical properties and the SCC resistance of these alloys. The authors attributed the enhancement in mechanical properties to mostly η' refinement, and the enhancement of SCC resistance to the coarsening and discrete spatial distribution of grain boundary precipitates (GB-ppts), as well as the increased Cu contents therein [7,15]. It should be noted that this age tempering protocol includes a T6 temper step, heat treatment at a higher temperature for a short period, followed by quenching in cold water, and finally re-aging at a lower temperature. Many steps are involved to complete the entire process, which significantly reduces its efficiency in industrial production.

To achieve lower industrial production costs and improved industrial efficiency, non-isothermal aging (NIA) has been widely used in the heat treatment of aluminum alloys, especially Al–Zn–Mg–Cu alloys [16]. Compared with conventional heat treatment, NIA can be completed with reduced time, thus increasing the production efficiency without material property loss [17]. A further optimized NIA process provided a higher strength and comparable SCC resistance to a standard T74 aging protocol [18]. They ascribed the changes to refined η' phase and the reduced width of PFZs [18]. For curved parts in aerospace vehicles, NIA applied during creep process could be a meaningful attempts to achieve both high strength and corrosion resistance with high producing efficiency [19,20]. Creep introduced during NIA has been designated as non-isothermal creep aging (NICA), and there is still a lack of systematic research on its influence on the microstructure, mechanical properties and SCC susceptibility of 7075 alloys.

Hence, this study systematical investigates the precipitation behavior, mechanical properties, and SCC resistance of 7075 alloys during NICA. The microstructures and microchemicals of the grain interior and grain boundaries were characterized by transmission electron microscopy (TEM), high-angle annular dark-field scanning transmission electron microscopy (HAADF-STEM) and energy dispersive spectroscopy (EDS). The mechanical properties and SCC of the alloys were tested by tensile and slow strain rate testing (SSRT) experiments.

2. Materials and methods

2.1. Materials

The chemical composition of the as received 7075 alloy has been analyzed using inductively coupled plasma mass spectrometry (ICP-MS). Table 1 summarizes the results. The alloy was solutionized at 470 °C for 0.5 h, followed by heat treatment at 475 °C and 480 °C for 0.5 h, respectively. After solid solutionization, high temperature pre-precipitation was carried out at 405 °C for 0.5 h, at a cooling rate of 30 °C/h, followed by quenching in cold water. Non isothermal creep aging was performed on the pre-precipitated alloy with a common heating/cooling rate. Sample IDs were assigned as CH and CC. In 'CH' series, the alloy is heated from room temperature to 120 °C, 160 °C or 210 °C at a rate of 20 °C/h. After reaching the temperature, samples were quenched in water to obtain CH120, CH160 or CH210 sample. In 'CC' series, all samples are heated from room temperature to 210 °C at the rate of 20 °C/h, then cooled to 100 °C, 120 °C or 160 °C at the same rate, and then quenched in water. The samples are designated as CC100, CC120 and CC160. An axial tensile load of 200 MPa was applied on the samples during the course of heating and cooling stage. The schematic diagram of the experimental process is shown in Fig. 1.

Table 1
Chemical composition of the as-received 7075 alloy.

	Zn	Mg	Cu	Zr	Si	Fe	Al
wt.%	5.66	2.34	1.82	0.09	0.16	0.08	Bal.

2.2. Microstructure characterization

Microstructure at locations within grains and at grain boundaries was characterized using scanning/transmission electron microscopy (S/TEM) and energy dispersive X-ray spectroscopy (EDS). Prior to testing, the age-treated sheet samples of CH120, CH210 and CC120 were mechanically thinned to 80−100 μm in thickness with mesh sizes of 400, 600, 800 and 1200, respectively. Φ 3 mm discs were punched from these thinned sheets. They were then twin-jet-electropolished at 17 V/−20 °C, using HNO_3 (25 vol%) in methanol. Bright field micrographs and selected area diffraction patterns were recorded on a FEI Tecnai $G^2$20, operated at 200 kV. High angle annular dark field imaging (HAADF) was carried out on a FEI Titan $G^2$60-300, operated at 300 kV in STEM mode.

2.3. Mechanical property

Tensile testing was carried out at room temperature on a MTS landmark 810 electronic universal testing machine. The loading rate measured 2 mm/min. Samples of L-T orientation were adopted, and were machined according to the Chinese National Standard GB/T228.1–2002 [21]. Three measurements were made per each aging condition, providing data regarding the yield strength ($\sigma_{0.2}$, MPa) and the ultimate tensile strength (σ_{UTS}, MPa).

2.4. Stress corrosion cracking (SCC)

The SCC susceptibility (I_{SCC}) of the 7075 alloy was evaluated with respect to the heating stage and the cooling stage involved, via slow strain rate testing (SSRT). SSRT was performed at a strain rate of 1.0×10^{-6} s^{-1} at room temperature, in either air or 3.5 wt% NaCl solution (corrosive environment). Prior to testing, all samples were polished and dried in air. The samples were loaded along the L-T direction. Results of evaluation included relative time-to-failure and loss in ultimate tensile strength after SSRT in air and 3.5 wt% NaCl solution. Three measurements were made per each alloy aging condition.

3. Results and discussion

3.1. Mechanical properties

Tensile tests of the 7075 alloys were carried out during the NICA process. Fig. 2 summarizes the results. The ultimate tensile strength (σ_{UTS}, MPa) and the yield strength ($\sigma_{0.2}$, MPa) were measured 524 MPa and 432 MPa, respectively, for CH120 alloy. These properties were further improved to 565 MPa and 493 MPa, respectively, for CH210 alloy. σ_{UTS} and $\sigma_{0.2}$ increased by 41 MPa and 61 MPa, respectively, during the heating stage. Both of these two kinds of strength reached 580 MPa and 512 MPa, respectively, after cooling from 210 °C (CH210) to 120 °C (CC120), and then keep nearly stable when the alloy cooled to 100 °C (CC100). Slightly decrease of elongation could be observed

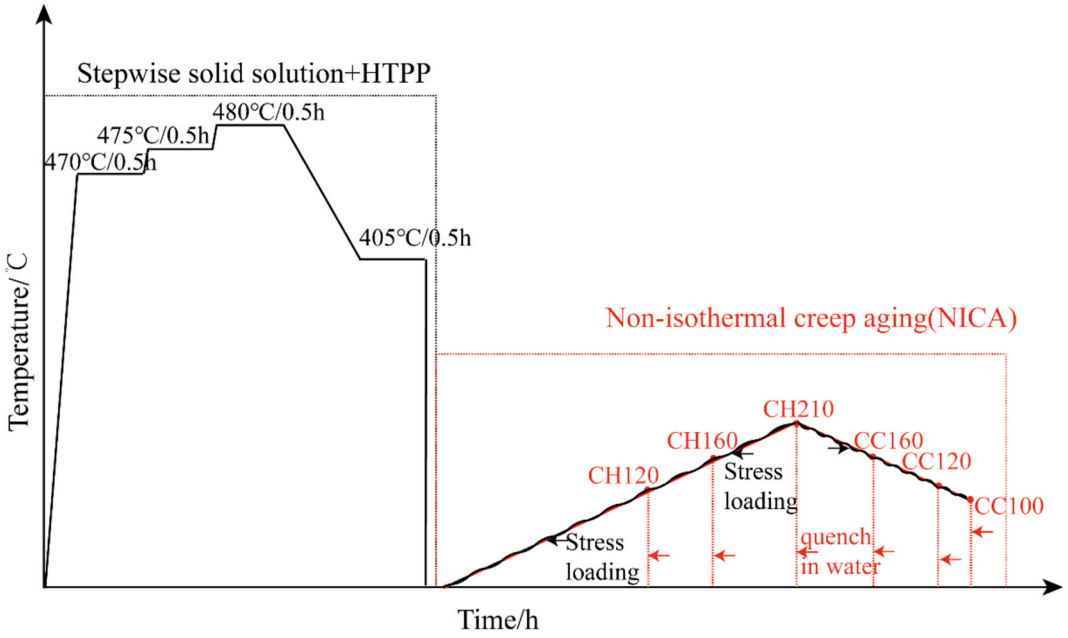

Fig. 1. Schematic diagram of the experimental process.

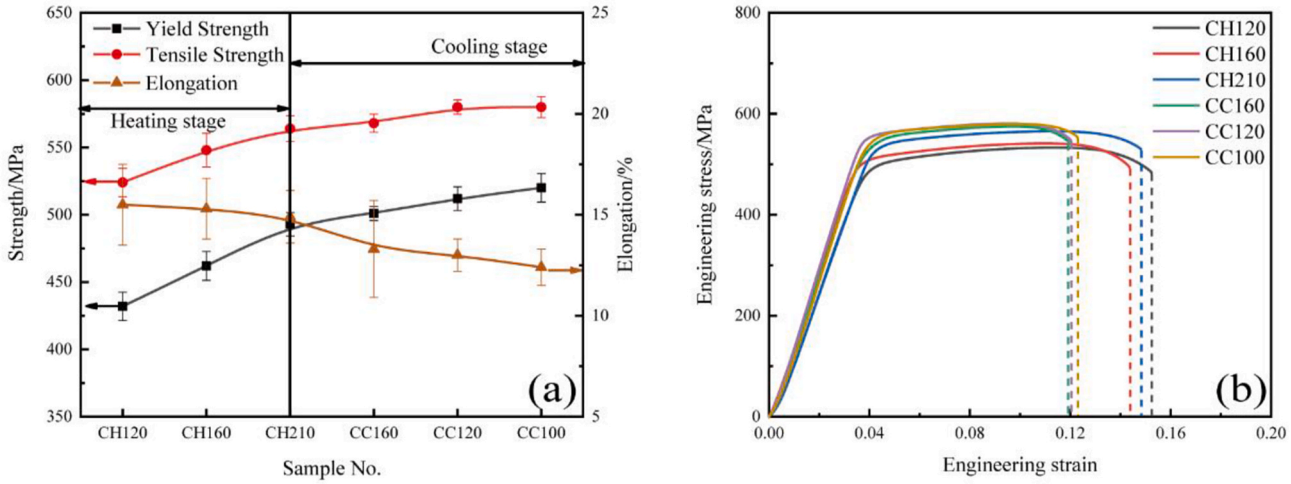

Fig. 2. Tensile strength, yield strength and elongation evolution of alloy (a) and corresponding stress-strain curves (b) during NICA process.

during the heating and cooling stage. Compared with traditional T6, T73, RRA and CAF process, a remarkable strength improvement and production time savings could be achieved by CC120 process, as shown in Table 2.

Table 2
The strength and production time cost of 7075 alloy with different aging process.

Aging process	Tensile strength (MPa)	Yield strength (MPa)	Production schedule	Ref.
T6	559	504	24 h@120 °C	[22]
T73	528	465	24 h@120 °C + 30 h@160 °C	[22]
RRA	568	512	24 h@120 °C + 10min@120 °C + 24 h@120 °C	[22]
CAF	535	470	24 h@150 °C+6 h@190 °C	[4]
CC120	580	512	13.5 h.	In our study

3.2. Microstructure in the grain interior

In general, types, size and distribution of precipitates in the grain interior play a significant role on the mechanical evolution for alloy. The reported precipitates responsible for strengthening in the 7075 alloy are GPI, GPII, η′ and η phases [23–26]. GPI features spherical morphology, ranging from 1 nm to 3 nm in size, and is coherent with the matrix [25,27]. The projection of the anti-phase structure of GPI consisting of Zn and Mg (or Al) atoms along the $[100]_{Al}$ direction is very similar to that of AuCuI. The produced patterns along $[100]_{Al}$ always display an internal order of four doublings of the Al structure along certain cubic directions with diffuse spots at $(1, (2n+1)/4, 0)_{Al}$ [28]. GPII phases form a thin plate on $\{111\}_{Al}$ planes with a chemical composition of Al, Zn, and Mg, and are correlated with diffraction streaks across $(111)_{Al}$ spots. The precipitation of GPII significantly depends on the concentration of quenched-in vacancies [27]. η′ precipitates are hexagonal-structured platelets lying on $\{111\}_{Al}$ planes. Their orientation relationship with the matrix is $(0001)_{\eta'}//(111)_{Al}$ and $[1010]_{\eta'}//[011]_{Al}$. The lattice parameter relationship between η′ and the matrix obtained through the

simulation calculation is $d(0001)_{\eta'} = 6d(111)_{Al}$ and $d(1010)_{\eta'} = 3d(220)_{Al}$ [29,30].

Fig. 3a shows that the size of the precipitates shown is less than 3 nm, while the SAED in Fig. 3b very weak and diffuse diffraction spots at positions of $(1,1/4,0)_{Al}$ and $(1,7/4,0)_{Al}$ can be observed. The FFT (Fig. 4c and e) and corresponding IFFT (Fig. 4b and d) of zone 1 and zone 2 in Fig. 4a reveals that the precipitates coherent with the matrix and the FFT patterns are the same as those in Fig. 3b. The precipitates have been identified GPI and it should be predominant for strengthening in CH120, where the 7075 alloy experienced NICA at 120 °C. With increasing aging temperature to 210 °C, diffraction spots of GPI are almost disappeared. Strong diffraction intensity at $1/3\{220\}_{Al}$ and $2/3\{220\}_{Al}$ spots indicate that η′ became the predominant strengthening phase, and that most GPI could transform to η′ (Fig. 3d). The size of precipitates increases to approximately 8 nm (Fig. 3c). Moreover, weak diffraction intensities in correspondence with the η phase can also be found (Fig. 3d). When the alloy was cooled from 210 °C to 120 °C at a cooling rate of 20 °C/h, the bright field images and select area diffraction patterns along $[100]_{Al}$ zone axes are shown in Fig. 3e and f. Strong diffraction spots of η′ and weak diffraction pattern of η are observed. In addition to these two phases, the spots of GPI re-emerged. The FFT patterns and IFFT images of zone 1-zone 4 in Fig. 5(CC120) also confirmed GPI, η′ and η are predominant for strengthening. Different from the SEAD in Fig. 3f, very weak diffraction pattern at 2/3(220) of zone 2 could be observed. Stiller et al. ascribe it to GPII [24]. The dislocation arrays are observed in the 7075 alloy as indicated by '⊥' along the interface. This suggests that the GPII, η′ and η precipitate is semi-coherent with the Al matrix. The size of the precipitates increased significantly during the heating stage and decreased during the cooling stage.

The precipitation process of an alloy is largely controlled by solute diffusion, the driving force and the nucleation energy barrier. The driving force Δg proposed by Aaronson is expressed as Eq. (1) [31]:

$$\Delta g = -\frac{kT}{v_{at}} ln\left(\frac{C}{C_{eq}}\right) \tag{1}$$

where v_{at} is the atomic volume of the precipitate, k is the Boltzmann's constant, T is the absolute temperature, C_{eq} is the equilibrium solute atomic concentration, and C is the current solute concentration of the matrix. The critical radius (R*) of the precipitates derived from the above equation is expressed as Eq. (2) [32]:

$$R^* = \frac{2\gamma v_{at}}{kTln\left(C/C_{eq}\right)} \tag{2}$$

where γ is the interface energy. Precipitates larger than the critical radius R* would be coarsened, and those smaller than R* would dissolve back into the matrix.

The precipitation sequence in Al–Zn–Mg–Cu alloys is SSS→GP zone → η′ → η. When the alloy is heated to 120 °C(CH120), the diffusion of Zn and Mg solutes accelerates, in favor of GPI formation. However, the size of GPI is too small that it could be cut by the moving dislocations and hinder the creep deformation. With aging temperature heated to 160 °C (CH160), the dislocations produced by creep could provide new nucleation sites for GPI (white arrows in Fig. 6a), and the driving force (Δg) in Equation (1) increases, which also favors precipitation. Furthermore, a lot of new dislocations have been produced in the matrix (the FFT of zone 1 in Fig. 6b is mainly composed by the matrix diffraction patterns and the corresponding IFFT of zone 1 indicates that a majority of '⊥' dislocations could be observed), which could provide new nucleation site for GPI and accelerate the diffusion of solutes for the following step. Hence, with continuous aging temperature increase to 210 °C(CH210), the new formed and metastable GPI transforms to more stable η′ by favored diffusion of solutes and Δg, as shown in Fig. 3c and d. The continuous precipitation and transformation take responsible for the improvement of mechanical properties during the heating stage. When the alloy cooled from 210 °C to 120 °C, the critical radius R* would increase with decreasing aging temperature with maximum v_{at} and a constant γ of η′. The fraction of precipitates with dimensions smaller than R* increases, and those precipitates dissolve back into the matrix. Simultaneously, secondary precipitation occurs owing to reduced solute

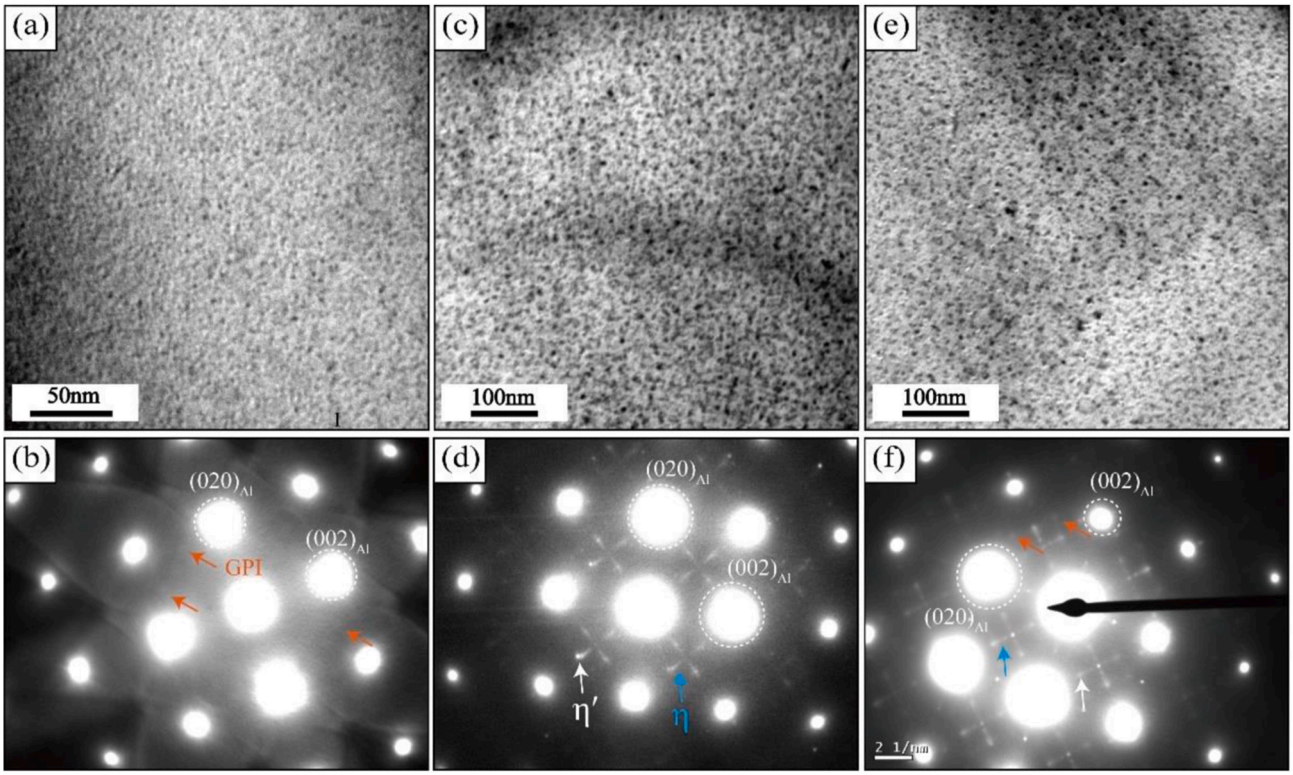

Fig. 3. Bright field images (a, c, e) and select area diffraction pattern (b, d, f) of CH120 (a,b), CH210 (c,d) and CC120 (e, f) viewed along $[100]_{Al}$ zone axes.

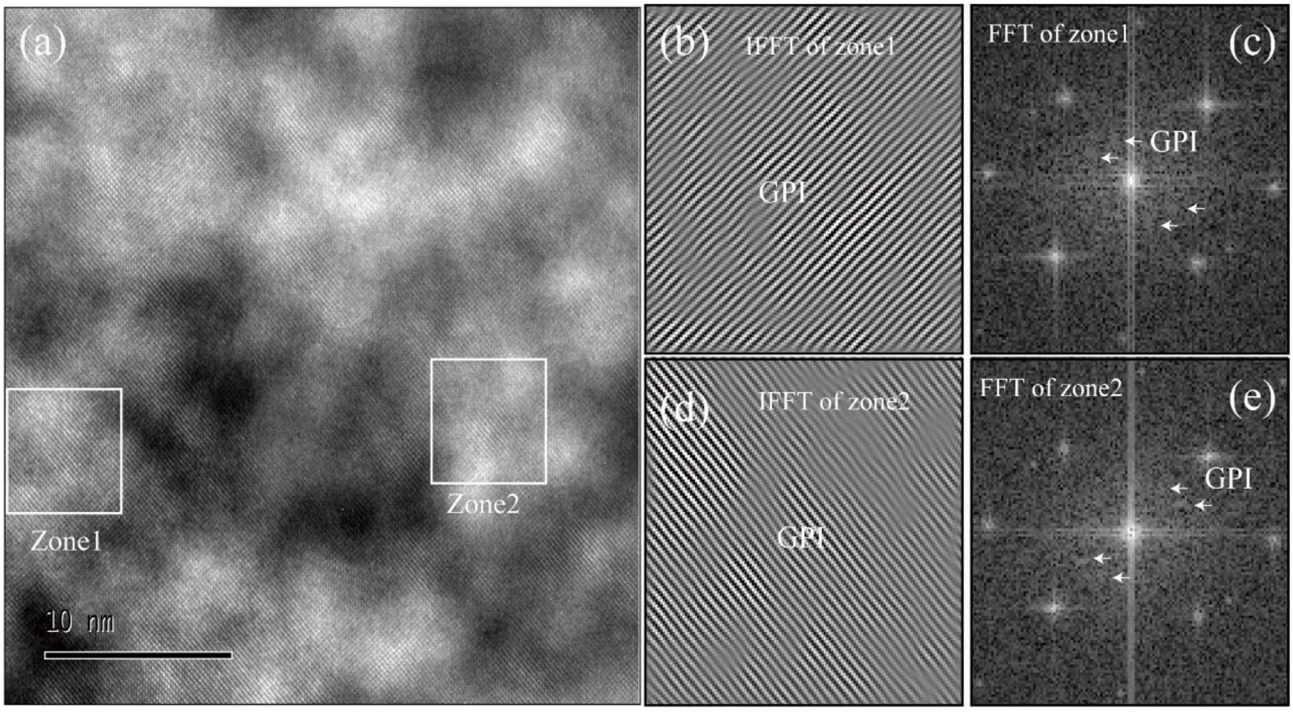

Fig. 4. HRTEM image (a), the IFFT pattern (b,d) and FFT image (c,e) of zone 1(b, c) and zone 2 (d,e) of CH120 alloy viewed along $[100]_{Al}$ zone axes.

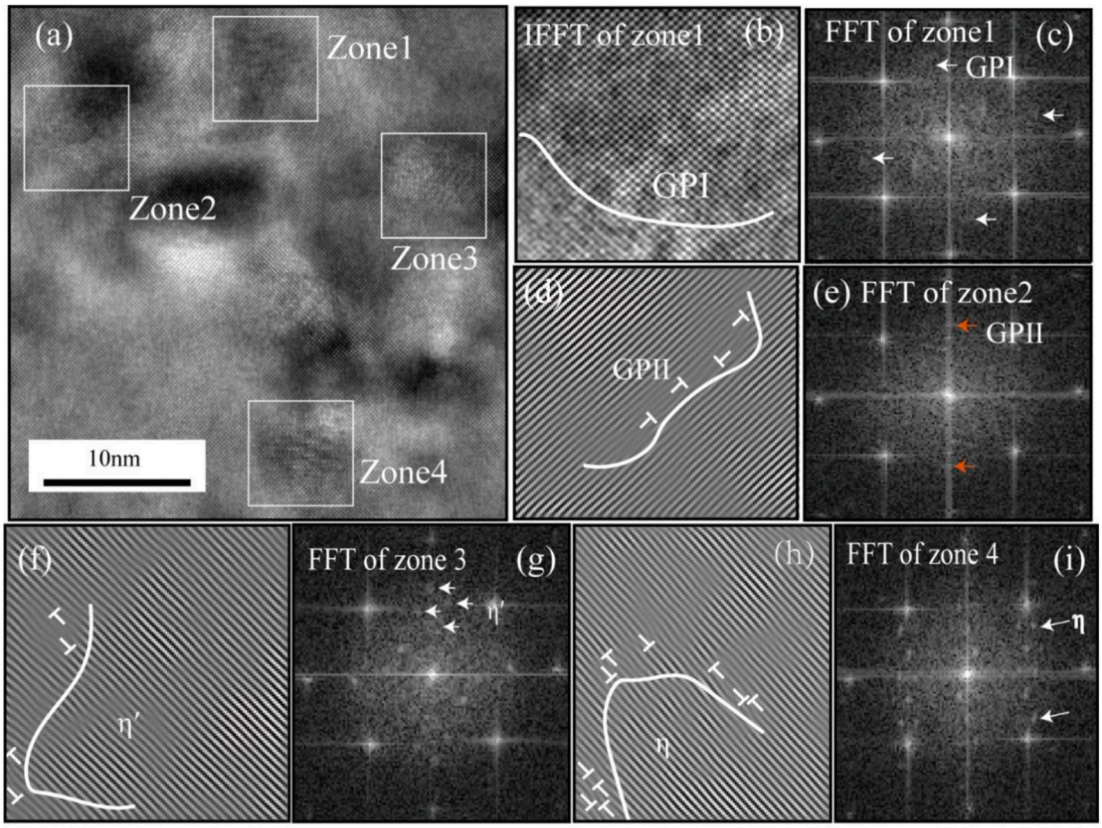

Fig. 5. HRTEM image (a), the IFFT pattern (b,d,f,h) and FFT image (c,e,g,i) of zone 1(b,c), zone 2 (d,e), zone 3(f,g) and zone 4 (h,i) of CC120 alloy viewed along $[100]_{Al}$ zone axes.

solubility in the matrix with decreasing temperature. The diffraction patterns of GPI could be observed again in Figs. 3f and Fig. 5a–c, and GPII could only be observed in CC120 alloy in Fig. 5d and e due to its small volume fraction. As compared with alloy treated by traditional T6, CAF and RRA [4,22,33], the size of η′ was remarkably refined and the density was improved in CC120 alloy. More importantly, GPI take

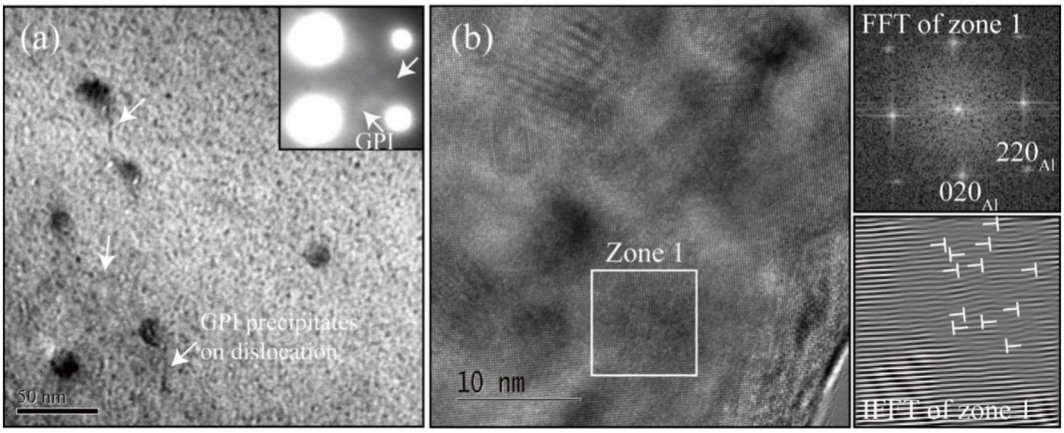

Fig. 6. Bright field image with selected area diffraction pattern (a), HRTEM image (b) and the corresponding FFT and IFFT image of zone 1 of CH160 alloy viewed along $[100]_{Al}$ zone axes.

responsible for strengthening again, which could further improve the mechanical properties of the alloy.

3.3. SCC susceptibility

Besides the mechanical property, stress corrosion cracking (SCC) is the most severe corrosion failure. It always breaks suddenly during service, which leads to accidents and serious threats to safety. Fig. 7 shows the stress–strain curves of the slow strain rate test (SSRT) of samples with CH120, CH160, CH210, CC160, and CC120 tempers in air and in 3.5 wt% NaCl solution. The tensile properties of CH120, CH160, CH210, CC160 and CC120 samples in both air and 3.5 wt% NaCl solution increased dramatically, slowly reached maximum, followed by a slight decrease prior to fracture failure. The strength of sample CH120 quickly reached the maximum in the 3.5 wt% NaCl solution, followed by sudden fracture. This finding suggests that alloy subject to CH120 temper exhibits a high SCC susceptibility. SCC susceptibility can be estimated using the ratio r_{tf} (Eq. (3)),

$$r_{tf} = \frac{t_{fc}}{t_{fe}} \tag{3}$$

where t_{fc} and t_{fe} represent the time-to-failure (t_f) of the alloy tested in air and in 3.5 wt% NaCl solution, respectively. A high r_{tf} value indicates low SCC susceptibility. Moreover, the tensile strength loss in the corrosive solution can be also adopted to evaluate the SCC susceptibility, which can be calculated using Eq. (4):

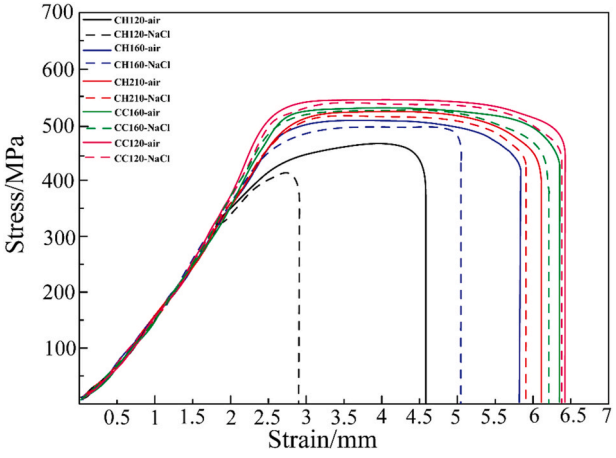

Fig. 7. SSRT tensile curves in air and in 3.5 wt% NaCl solution.

$$\text{Strength loss} = \frac{\sigma_{air} - \sigma_{NaCl}}{\sigma_{air}} \tag{4}$$

σ_{air} and σ_{NaCl} correspond to ultimate tensile strength in air and in 3.5 wt% NaCl solution, respectively. A lower strength loss indicates a lower SCC susceptibility. The tensile strength, strength loss, t_f and r_{tf} values of the 7075 alloy with different tempers are listed in Table 3. The strength loss of sample CH120 was 12.9 %, which was lowered to 7.8 % upon continuous heating to 160 °C (CH160). After heating to 210 °C (CH210), strength loss reached 1.7 % and did not show a significant decrease in the subsequent cooling stage (1.5 % for CC160 and 1.3 % for CC120). Evaluation of the relationship between strength loss and SCC susceptibility is limited. Another SCC susceptibility evaluation factor is the time-to-failure r_{tf}. Table 3 shows that the r_{tf} of CH120 was 50.8 % and reached 86.3 % after the alloy was continuously heated to 210 °C (CH210). During the cooling stage, r_{tf} reached 96.9 % (CC160) and 98.4 % (CC120). In this study, r_{tf} was more sensitive and effective for the evaluation of SCC susceptibility. Sample CC120 exhibited the best SCC resistance.

The corresponding fracture topography of the alloy with CH120, CH210 and CC120 after SSRT has been characterized by SEM, as shown in Fig. 8. It can be observed from Fig. 8a, c and e that the surface and the subsurface areas belong to the intergranular fracture mode, and the interior of the alloy belongs to the ductile fracture mode. Choi et al. considered that this type of intergranular fracture is caused by SCC, and the internal ductile fracture plays a major role in the mechanical properties of the alloy [34]. The area of SCC regions in Fig. 8a, c and e follows as the same order (CH120>CH210>CC120) as the SCC susceptibility of the above. The magnified SEM image of SCC region in Fig. 8a shows that the fracture morphology in this area is a typical candy-like brittle fracture (Fig. 8b), which indicates the grain-boundary has been attacked seriously and results in the whole grain depart from the other. Different from the CH120, dimples could be found in the grain interior in Fig. 8d

Table 3
Mechanical properties and time to failure of alloys after SSRT testing.

Sample No.	Environment	UTS/MPa	Strength loss	t_f/s	r_{tf}
CH120	In air	482	12.9 %	233667	50.8 %
	3.5 wt% NaCl	420		118755	
CH160	In air	513	7.8 %	211064	59.2 %
	3.5 wt% NaCl	473		124876	
CH210	In air	529	1.7 %	251976	86.3 %
	3.5 wt% NaCl	520		217633	
CC160	In air	536	1.5 %	264797	96.9 %
	3.5 wt% NaCl	528		256486	
CC120	In air	543	1.3 %	274370	98.4 %
	3.5 wt% NaCl	536		270211	

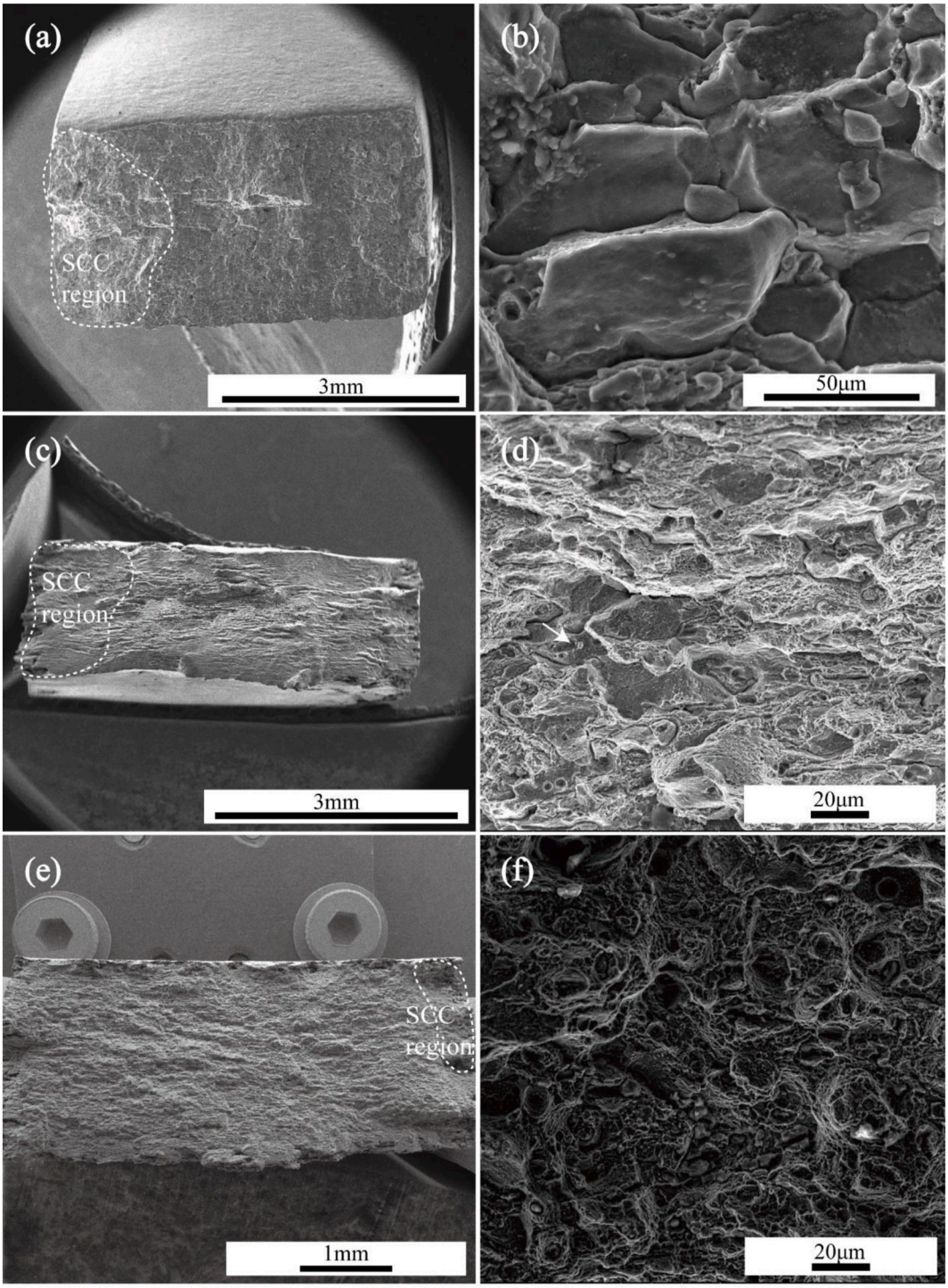

Fig. 8. Fracture topography of alloy and the corresponding magnified SCC region with CH120(a,b), CH210(c,d) and CC120(e,f) after SSRT in 3.5 % NaCl solution.

and f, which indicates that the strength in the grain boundary and interior has been improved simultaneously.

3.4. Microstructure along the grain-boundary

Generally speaking, the stress crack corrosion can be divided into two processes: anodic dissolution and hydrogen embrittlement [35–37]. Anodic dissolution has been reported to be produced by the potential difference of PFZ, precipitates in the grain interior and grain-boundary when they were exposed in 3.5%NaCl solution after the oxide film was destroyed by stress loading, it takes responsible for the initial stage of SCC. The anodic dissolution processes can be described as follows [38]:

$$\mathrm{M(Metallic\ elements\ in\ the\ alloy)} \rightarrow \mathrm{M^{n+}} + \mathrm{ne^-} \tag{1a}$$

$$\mathrm{M^{n+}} + \mathrm{zH_2O} \rightarrow M(OH)_Z^{(n-z)+} + zH+ \tag{2a}$$

$$\mathrm{H^+ + e-} \rightarrow \mathrm{H_{ads}} \tag{3a}$$

$$\mathrm{H_{ads}} + \mathrm{H_{ads}} \rightarrow \mathrm{H_2} \tag{4a}$$

After the first stage of SCC, continuous stress loading exposes fresh

metal to the corrosive medium, causing hydrogen to continuously accumulate toward the crack tip. Hydrogen atoms form hydrogen gas. When the hydrogen gas pressure reaches a certain level, the crack expansion is accelerated. Hence, the electrochemical behavior of the microstructure along the grain-boundary is significant for the SCC in Al–Zn–Mg–Cu alloy. Fig. 9 reveals the microstructure of grain boundary of alloy with CH120 treatment, it can be seen that the precipitates distribute continuously along the grain-boundary (Fig. 9a) with size obviously coarser than that in the grain interior (Fig. 9b). Al, Cu, Mg and Zn are distributed homogeneously, as shown in Fig. 9c–f. Like the precipitates identified in Fig. 3, the coarser ones along the grain boundary could also be GPI composed by Zn and Mg solutes. According to the investigation of Birbilis et al., the corrosion potentials of Zn (−1028 mV/SCE in 3.5 wt% NaCl solution) and Mg (−1688 mV/SCE in 3.5 wt% NaCl solution) are more negative than the matrix (−812 mV/SCE in 3.5 wt% NaCl solution) [39]. It can be inferred that the GPI phase could be anodic and reactions of (1)-(4) occur when exposed in the electrolyte. Dissolution of continuous GPI forms corrosion channels and accelerates hydrogen accumulation, both of them deteriorate the strength of the grain-boundary. Moreover, coherent and fine GPI is difficult to hinder the movement of dislocations and can easily co-slip with the matrix, causing a large number of dislocations to accumulate at the grain boundaries, leading to further increase of SCC susceptibility. Hence, typical candy-like brittle fracture could be seen in Fig. 8a and b.

After NICA at 210 °C (CH210), precipitates located within grains and along grain boundaries were coarsened in the 7075 alloys. The coarsening of GB-ppts consumes solutes from the adjacent matrix, forming a (46.1 ± 3) nm wide PFZ. Both continuous and discontinuous precipitates can be observed in Fig. 10. Mg and Zn are segregated in the precipitates on the grain boundary, and significant Zn and slight Cu and Mg depletion can be observed in the adjacent PFZ in Fig. 10c–f. The elemental distribution indicates that the precipitates on the grain boundary should be η′ or η with a chemical composition of $MgZn_2$. The reported corrosion potential of $MgZn_2$ in 3.5%NaCl solution was −1095 mV/SCE and that of the PFZ was −812 mV/SCE [39]. Anodic dissolution could occur due to the remarkable potential difference between the GB-ppts and PFZ. Continuous dissolution could occur along the continuous distributed $MgZn_2$ particles and crack could propagate rapidly along these sites. Hence, intergranular fracture can also be observed in CH210 alloy after SSRT (Fig. 8c and d). Different from fracture surface of SCC region in CH120, a large number of dimples can be observed in the grain interior because the major strengthening phase evolved to dislocation hindered η′ (Fig. 3e and f). The dissolution and crack propagation could be slowed down when they come across with discontinuous $MgZn_2$ particles, and coarse $MgZn_2$ precipitates act as H trapping sites. Both of them can lower SCC susceptibility for CH210 alloy. Therefore, the SCC resistance was dramatically improved as r_{tf} increased from 50.8 % (CH120) to 86.3 % (CH210).

During the cooling stage, the critical radius R* increases with decreasing aging temperature, which leads to the dissolution of larger precipitates on the grain boundary. The precipitate size is significantly reduced, and secondary precipitation is observed along the grain boundary and nearby (Fig. 11b). The width of the PFZ is reduced to 28.6 ±3 nm (Fig. 11a), which is significantly smaller than 70 nm of 7075 alloy treated by isothermal aging and RRA during creep [4]. Moreover, precipitates along grain boundaries are distributed discontinuous. EDS mapping of Figs. 11e–f reveals that precipitates at grain boundaries are enriched in Mg and Zn, which could also represent $MgZn_2$ particles. The solutes are distributed more homogeneously than those in sample CH210, as shown in Fig. 11c–f. Although the size of $MgZn_2$ at the grain boundary is reduced, it could still act as a H trapping site. A narrower PFZ width and discontinuous distribution of $MgZn_2$ can counter-balance the weakening of the H-trapping capacity caused by the refinement of the size of GB-ppts, and effectively lower the material's SCC susceptibility. The area of SCC region in CC120 alloy remarkably smaller that of CH120 and CH210 alloy (Fig. 8e and f). The r_{tf} value of sample CC120

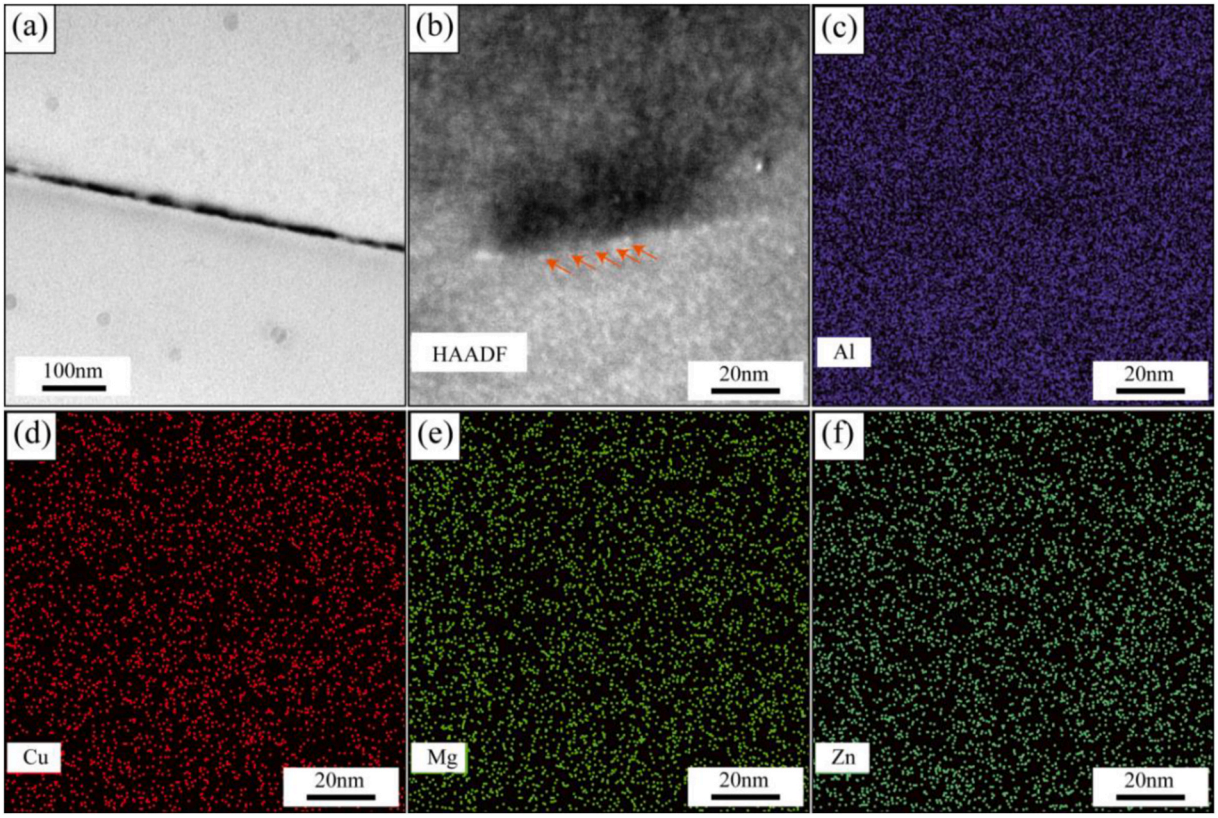

Fig. 9. HAADF-STEM image(a-b), EDS maps of Al(c), Cu(d), Mg(e) and Zn(f) of the CH120 alloy. Electron beam direction://$[001]_{Al}$.

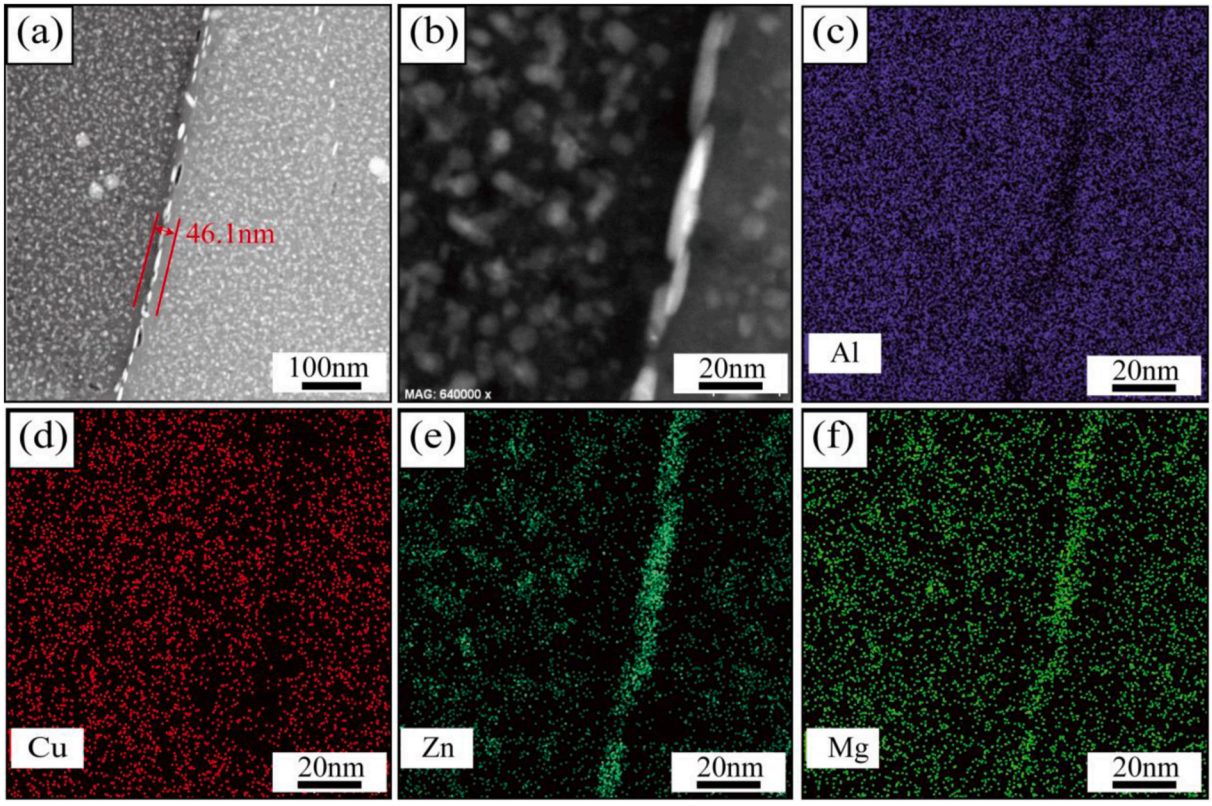

Fig. 10. HAADF-STEM image(a-b), EDS maps of Al(c), Cu(d), Zn(e) and Mg(f) of CH210 alloy. Electron beam direction://$[001]_{Al}$.

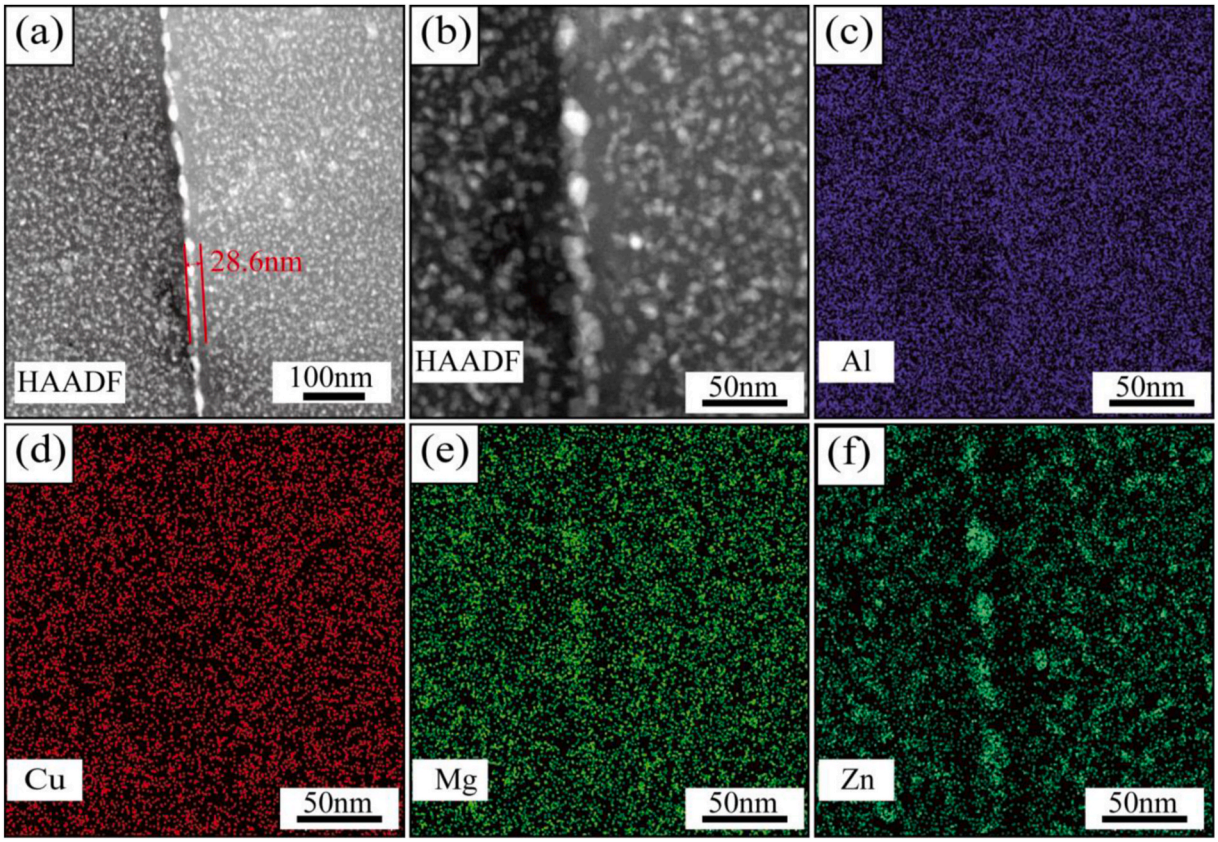

Fig. 11. HAADF-STEM image (a–b), EDS maps of Al(c), Cu(d), Mg(e) and Zn(f) of CC120 alloy. Electron beam direction://$[001]_{Al}$.

increased to 98.4 %, exhibiting the best SCC resistance among all samples examined.

Besides the mentioned above, the microchemistry of GB-ppts, PFZ, M-ppts and the matrix could be another key point for SCC susceptibility in Al–Zn–Mg–Cu alloy. It can be seen in Fig. 12 and Table 4 that: (1) the Cu content in GB-ppts and PFZ is higher in CC120 than in CH210; (2) the Mg content in GB-ppts in CC120 is lower than in CH210; (3) the concentration difference of active Mg and Zn solutes between the GB-ppts and PFZ in CC120 alloy is smaller than that in CH210 alloy; (4) the concentration difference of active Mg and Zn solutes between the grain interior (composed be M-ppts and matrix) and grain boundary (composed by GB-ppts and PFZ) of CC120 alloy is also smaller than that in CH210 alloy. Generally, Mg can enhance the absorption of H and increase the H content along grain boundaries via Mg–H interactions [40–42]. The reduction of Mg content in the GB-ppts of CC120 would reduce the formation of Mg–H complexes and lower its SCC susceptibility from hydrogen embrittlement. Furthermore, increasing Cu content in the GB-ppts and PFZ in CC120 could render them less electrochemically active, and reduce the rate of anodic dissolution and cathodic H production at crack tips [43,44]. Active Mg and Al from the GB-ppts dissolve and leave behind a Cu rich remnant which detaches from the matrix and dissolves in the electrolytic solution as Cu ions. These ions can re-plate and re-precipitate on the surface to avoid further corrosion [45]. Moreover, the reduced concentration difference of active Mg and Zn solutes in CC120 alloy between the grain boundary and grain interior, the GB-ppts and PFZ could lower the driving force for anodic dissolution during SCC. Hence, CC120 exhibits the most excellent SCC resistance.

Table 4
Atomic percentage content of Al, Zn, Cu and Mg in GB-ppts, PFZ, M-ppts and matrix in the 7075 alloy.

Point		Position	Al(at%)		Zn(at%)		Mg(at%)		Cu(at%)	
H210	C120		H210	C120	H210	C120	H210	C120	H210	C120
1	5	GB-ppts	77.29	79.92	11.8	10.42	8.89	7.33	2.02	2.33
2	6	PFZ	96.39	95.29	1.81	1.03	0.96	2.07	0.94	1.61
3	7	M-ppts	81.76	83.92	10.41	8.63	6.42	5.93	1.41	1.52
4	8	Matrix	96.39	94.32	1.01	1.52	1.22	2.53	1.38	1.63

4. Conclusions

The effects of non-isothermal creep aging on the microstructure, mechanical properties and SCC were systematically investigated for the 7075 alloy. Key conclusions are summarized as follows:

(1) The strength and SCC resistance improved during the heating and cooling stages. Alloys creep aged at 210 °C followed by cooling to 120 °C (CC120) exhibited the highest strength and best SCC resistance.

(2) During the heating stage, the major precipitate responsible for strengthening in alloy CH120 was GPI, which then evolved to η′ with a small amount of η in alloy CH210. The precipitation could be greatly improved with the help of dislocations introduced by creep. During the cooling stage, the alloy was strengthened by phases of η′, GPI, GPII and η. Particles with sizes larger than R* can dissolve into the matrix and lead to secondary precipitation, refining the precipitate size and increasing the precipitate density. Alloy CC120 exhibited the best combination of mechanical properties.

(3) The GPI phase distributed continuously on the grain boundaries in alloy CH120, and transformed to coarse η′/η phases. Both continuous and discontinuous precipitate distributions were observed in CH210 and a PFZ was formed. During cooling stage, the precipitate distributions appeared discontinuous, the size of GB-ppts was refined, and the width of the PFZ was reduced due to secondary precipitation.

(4) In alloy CC120, solutes were distributed more homogeneously, reducing the driving force for electrochemical corrosion. More importantly, the Cu content increased slightly in the GB-ppts of CC120. Combined with the effect of narrowed width of PFZs, significant reduction in the SCC susceptibility of alloy CC120 was achieved.

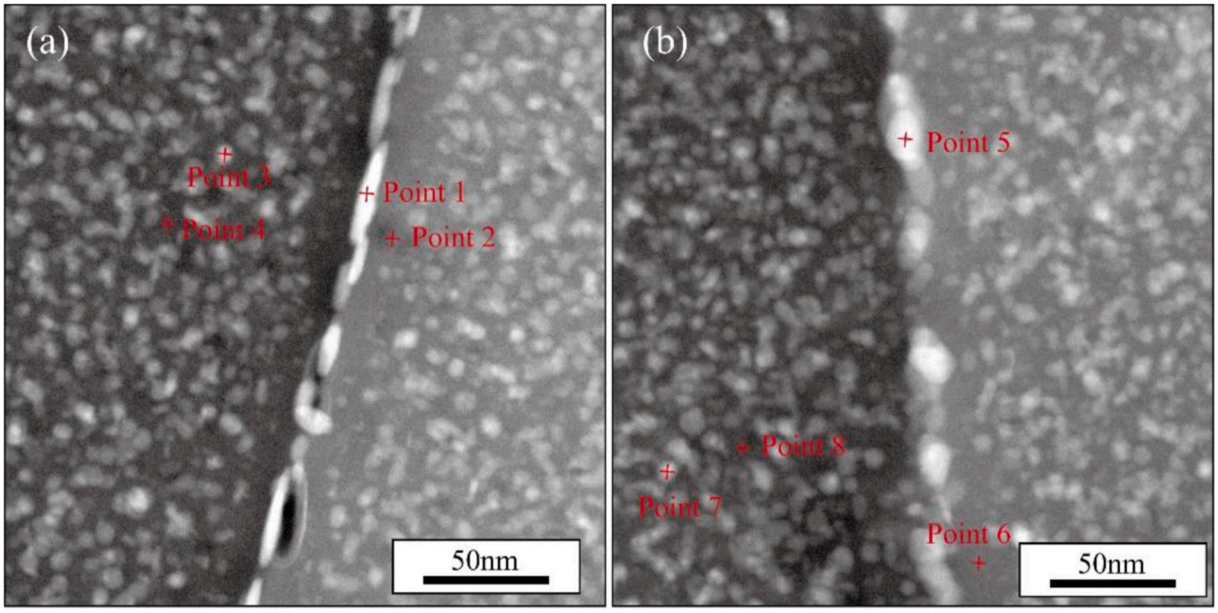

Fig. 12. Grain boundary HAADF-STEM images of NICA-treated the 7075 alloy: (a) CH210; (b) CC120.

Data availability

Data will be made available on request.

Declaration of competing interest

We declare that we have no financial and personal relationships with other people or organizations that can inappropriately influence our work, there is no professional or other personal interest of any nature or kind in any product, service and/or company that could be construed as influencing the position presented in, or the review of, the manuscript entitled “Effect of non-isothermal creep aging on the microstructure, mechanical properties and stress corrosion cracking resistance of 7075 alloy”.

Acknowledgements

The authors thank the program of the National Natural Science Foundation of China (Project No.: 52001033, 12102433), the Innovation and Entrepreneurship Program of Jiangsu Province of China (Project No. JSSCBS20210878), Research and industrialization of high-performance nitrogen and oxygen sensor chips for the automotive industry (Project No: HK2021004) for financial support.

References

[1] Chen S, Chen K, Dong P, Ye S, Huang L. Effect of recrystallization and heat treatment on strength and SCC of an Al-Zn-Mg-Cu alloy. J Alloys Compd 2013;581:705–9. https://doi.org/10.1016/j.jallcom.2013.07.177.
[2] Deng Y, Ye R, Xu G, Yang J, Pan Q, Peng B, et al. Corrosion behaviour and mechanism of new aerospace Al – Zn – Mg alloy friction stir welded joints and the effects of secondary Al 3 Sc x Zr 1 À x nanoparticles. Corrosion Sci 2015;90:359–74. https://doi.org/10.1016/j.corsci.2014.10.036.
[3] Arabi Jeshvaghani R, Emami M, Shahverdi HR, Hadavi SMM. Effects of time and temperature on the creep forming of 7075 aluminum alloy: springback and mechanical properties. Mater Sci Eng 2011;528:8795–9. https://doi.org/10.1016/j.msea.2011.08.025.
[4] Arabi Jeshvaghani R, Zohdi H, Shahverdi HR, Bozorg M, Hadavi SMM. Influence of multi-step heat treatments in creep age forming of 7075 aluminum alloy: optimization for springback, strength and exfoliation corrosion. Mater Char 2012;73:8–15. https://doi.org/10.1016/j.matchar.2012.05.012.
[5] Knight SP, Birbilis N, Muddle BC, Trueman AR, Lynch SP. Correlations between intergranular stress corrosion cracking, grain-boundary microchemistry, and grain-boundary electrochemistry for Al-Zn-Mg-Cu alloys. Corrosion Sci 2010;52:4073–80. https://doi.org/10.1016/j.corsci.2010.08.024.
[6] Sha G, Yao L, Liao X, Ringer SP, Duan ZC, Langdon TG. Segregation of solute elements at grain boundaries in an ultrafine grained Al-Zn-Mg-Cu alloy. Ultramicroscopy 2011;111:500–5. https://doi.org/10.1016/j.ultramic.2010.11.013.
[7] Peng G, Chen K, Chen S, Fang H. Influence of repetitious-RRA treatment on the strength and SCC resistance of Al-Zn-Mg-Cu alloy. Mater Sci Eng 2011;528:4014–8. https://doi.org/10.1016/j.msea.2011.01.088.
[8] Marlaud T, Deschamps A, Bley F, Lefebvre W, Baroux B. Evolution of precipitate microstructures during the retrogression and re-ageing heat treatment of an Al-Zn-Mg-Cu alloy. Acta Mater 2010;58:4814–26. https://doi.org/10.1016/j.actamat.2010.05.017.
[9] Peng X, Guo Q, Liang X, Deng Y, Gu Y, Xu G, et al. Mechanical properties, corrosion behavior and microstructures of a non-isothermal ageing treated Al-Zn-Mg-Cu alloy. Mater Sci Eng 2017;688:146–54. https://doi.org/10.1016/j.msea.2017.01.086.
[10] ling Yuan D, yi Chen S, hua Chen K, ping Huang L, yu Chang J, Zhou L, et al. Correlations among stress corrosion cracking, grain-boundary microchemistry, and Zn content in high Zn-containing Al–Zn–Mg–Cu alloys. Trans Nonferrous Metals Soc China 2021;31:2220–31. https://doi.org/10.1016/S1003-6326(21)65650-9.
[11] M.O. Speidel, M. V Hyatt, M.O. Speidel, M. V Hyatt, Stress corrosion cracking of high strength aluminum alloys, (n.d.).
[12] Knight SP, Pohl K, Holroyd NJH, Birbilis N, Rometsch PA, Muddle BC, et al. Some effects of alloy composition on stress corrosion cracking in Al-Zn-Mg-Cu alloys. Corrosion Sci 2015;98:50–62. https://doi.org/10.1016/j.corsci.2015.05.016.
[13] Meng Q, Frankel GS. Effect of Cu content on corrosion behavior of 7xxx series aluminum alloys. J Electrochem Soc 2004;151:B271. https://doi.org/10.1149/1.1695385.
[14] Cina B. Reducing the susceptibility of alloy, particularly aluminum alloys to stress corrosion cracking. Washington, DC: US Patent Office; 1974. p. 24. Pat. 3856584.
[15] Zhao H, Gault B, Ponge D, Raabe D. Reversion and re-aging of a peak aged Al-Zn-Mg-Cu alloy. Scripta Mater 2020;188:269–73. https://doi.org/10.1016/j.scriptamat.2020.07.049.
[16] Staley James T., Method and process of non-isothermal aging for aluminum alloys. WO,US2007267113A1.
[17] Li S, Dong H, Li P, Chen S. Effect of repetitious non-isothermal heat treatment on corrosion behavior of Al-Zn-Mg alloy. Corrosion Sci 2018;131:278–89. https://doi.org/10.1016/j.corsci.2017.12.004.
[18] Jiang JT, Tang QJ, Yang L, Zhang K, Yuan SJ, Zhen L. Journal of materials processing technology non-isothermal ageing of an Al – 8Zn – 2Mg – 2Cu alloy for enhanced properties. J Mater Process Technol 2016;227:110–6. https://doi.org/10.1016/j.jmatprotec.2015.07.018.
[19] Liu G, Lin YC, Zhang XC, Jiang YQ. Effects of two-stage creep-aging on precipitates of an Al-Cu-Mg alloy. Mater Sci Eng 2014;614:45–53. https://doi.org/10.1016/j.msea.2014.07.014.
[20] Xu L, Tong C, Zhan L, Xu Y, Liu C, Huang M, et al. Improved creep forming efficiency and retained performance via a novel two-stage creep aging process of Al–Zn–Mg–Cu alloys. Mater Sci Eng 2022:851. https://doi.org/10.1016/j.msea.2022.143581.
[21] G. 228-2002. Satandard, Metallic materials–Tensile testing at ambient temperature. 2002.
[22] Jin-feng LI, Zhuo-wei P, Chao-xing LI, Zhi-qiang JIA. Mechanical properties , corrosion behaviors and microstructures of 7075 aluminium alloy with various aging treatments. 2007.
[23] Berg LK, Gjonnes J, ansen VH, Li XZ. GP-zones in Al-Zn-Mg alloys and their role in artificial ageing. Acta Mater 2001;49:3443–51. https://doi.org/10.1109/ICFCC.2010.5497611. et-al.
[24] Stiller K, Warren PJ, Hansen V, Angenete J, Gjønnes J. Investigation of precipitation in an Al-Zn-Mg alloy after two-step ageing treatment at 100° and 150°C. Mater Sci Eng 1999;270:55–63. https://doi.org/10.1016/S0921-5093(99)00231-2.
[25] Hansen V, Karlsen OB, Langsrud Y, Gjønnes J. Precipitates, zones and transitions during aging of Al - Zn - Mg - Zr 7000 series alloy. Mater Sci Technol 2004;20:185–93. https://doi.org/10.1179/026708304225010424.
[26] Sha G, Cerezo A. Characterization of precipitates in an aged 7xxx series Al alloy. Surf Interface Anal 2004;36:564–8. https://doi.org/10.1002/sia.1702.
[27] Mukhopadhyay AK. Guinier-preston zones in a high-purity al-zn-mg alloy. Phil Mag Lett 1994;70:135–40. https://doi.org/10.1080/09500839408240966.
[28] Schmalzried H, Gerold V. Age-hardening in an Al-Mg-Zn alloy. Z Metallkd 1958;49:291–301.
[29] Wu L, Seyring M, Rettenmayr M, Wang W. Characterization of precipitate evolution in an artificially aged Al – Zn – Mg – Sc – Zr alloy. Mater Sci Eng, A 2010;527:1068–73. https://doi.org/10.1016/j.msea.2009.09.023.
[30] Liu JZ, Chen JH, Yang XB, Ren S, Wu CL, Xu HY, et al. Revisiting the precipitation sequence in Al-Zn-Mg-based alloys by high-resolution transmission electron microscopy. Scripta Mater 2010;63:1061–4. https://doi.org/10.1016/j.scriptamat.2010.08.001.
[31] Aaronson HI, Kinsman KR, Russell KC. The volume free energy change associated with precipitate nucleation. Scripta Metall 1970;4:101–6.
[32] Deschamps A, Brechet Y. Influence of predeformation and ageing of an Al-Zn-Mg Alloy-II. Modeling of precipitation kinetics and yield stress. Acta Mater 1998;47:293–305. https://doi.org/10.1016/S1359-6454(98)00296-1.
[33] Park JK, Ardell AJ. Effect of retrogression and reaging treatments on the microstructure of Al-7075-T651. Metall Trans A 1984;15:1531–43. https://doi.org/10.1007/BF02657792.
[34] Pyun S. Stress corrosion cracking of Al-Zn-Mg alloy AA-7039 by slow strain-rate method 1984;19:1517–21.
[35] Dey S, Chattoraj I. Interaction of strain rate and hydrogen input on the embrittlement of 7075 T6 Aluminum alloy. Mater Sci Eng 2016;661:168–78. https://doi.org/10.1016/j.msea.2016.03.010.
[36] Hardwick DA, Thompson AW, Bernstein IM. The effect of copper content and heat treatment on the hydrogen embrittlement of 7050-type alloys. Corrosion Sci 1988;28:1127–37. https://doi.org/10.1016/0010-938X(88)90123-0.
[37] Zhi GUOYH, Guo JIN, Gan T. Research prospect of stress corrosion of aeronautical aluminum alloys. 2020. p. 4–7. https://doi.org/10.16581/j.cnki.issn1671-3206.20200110.038.
[38] Takahashi K, Maruo Y, Kitamori T, Shimura K. Influence of critical surface defects and localized competition between anodic dissolution and hydrogen effects during stress corrosion cracking of a 7050 aluminium alloy. Mater Sci Eng, A 1997;239:293–302. https://doi.org/10.1002/jssc.200800609.
[39] Birbilis N, Buchheit RG. Electrochemical characteristics of intermetallic phases in aluminum alloys : an experimental survey and discussion. J Electrochem Soc 2005;152:140–51. https://doi.org/10.1149/1.1869984.
[40] Zhao H, Chakraborty P, Ponge D, Hickel T, Sun B, Wu CH, et al. Hydrogen trapping and embrittlement in high-strength Al alloys. Nature 2022;602:437–41. https://doi.org/10.1038/s41586-021-04343-z.
[41] Viswanadham RK, Sun TS, Green JAS. Grain boundary segregation in Al-Zn-Mg alloys—implications to stress corrosion cracking. Metall Mater Trans 1980;11:85–9.
[42] Song RG, Tseng MK, Zhang BJ, Liu J, Jin ZH, Shin KS. Grain boundary segregation and hydrogen-induced fracture in 7050 aluminium alloy. Acta Mater 1996;44:3241–8. https://doi.org/10.1016/1359-6454(95)00406-8.

[43] Jones DA. Principles and prevention of corrosion. Upper Saddle River, New Jersey: Prentice Hall, Inc; 1996.
[44] Ramgopal T, Gouma PI, Frankel GS. Role of grain-boundary precipitates and solute-depleted zone on the intergranular corrosion of aluminum alloy 7150. Corrosion 2002;58:687–97. https://doi.org/10.5006/1.3287699.
[45] Jiang B, Wang H, Tian Y, Yi D, Liu H, Hu Z. Effects of aging time on corrosion behavior of an Al-Cu-Li alloy. Corrosion Sci 2020;173:108759. https://doi.org/10.1016/j.corsci.2020.108759.